communications earth & environment

Article

A Nature Portfolio journal

https://doi.org/10.1038/s43247-026-03317-1

Carbon neutrality timing controls future tropical cyclone intensity and precipitation over the western North Pacific

Minkyu Lee[1], Seung-Ki Min[2] ✉ & Dong-Hyun Cha[3]

This study examines how different global warming levels associated with near-future carbon neutrality timings influence future tropical cyclone activity over the western North Pacific, using a pseudo-global warming framework. Convection-permitting simulations of multiple landfalling tropical cyclones were performed with the Weather Research and Forecasting model under two Shared Socioeconomic Pathways: SSP1-1.9 and SSP1-2.6, corresponding to net-zero emissions in the 2050 s and 2070 s, respectively. Delayed attainment of net-zero emissions leads to more substantial intensification, with the area affected by strong winds expanding by 7% and 9%, and regions of heavy precipitation by 15% and 22%, under SSP1-1.9 and SSP1-2.6, respectively. These differential responses are driven primarily by thermodynamic changes (atmospheric moisture increase) and also contributed by dynamic changes (enhanced vertical motion). The results underscore that the timing of carbon neutrality is a critical determinant of the severity of landfalling tropical cyclone impacts.

Tropical cyclones (TCs) are among the most destructive natural hazards, causing severe damage in coastal regions through strong winds, heavy precipitation, and storm surges, often leading to flooding, landslides, and other catastrophic impacts. TCs over the western North Pacific (WNP) account for roughly one-third of all TCs worldwide[1–3], rendering countries along the Asian coast particularly vulnerable[4]. Understanding how TC intensity and precipitation respond to global warming is critical. Warmer sea surface temperatures (SSTs) provide enhanced thermal energy for TCs, potentially increasing both their intensity and precipitation[5,6]. In addition, as atmospheric temperatures rise, the capacity of the atmosphere to hold moisture increases in accordance with the Clausius–Clapeyron relation[7–9], which predicts an approximate 7% increase in moisture content per 1 °C warming. Numerous studies have documented that TC-associated precipitation intensifies with rising temperatures[10–13]. For instance, Wright et al.[14] show that precipitation near the TC center can exceed Clausius–Clapeyron scaling, whereas it converges toward the scaling at larger azimuthal radii. Similarly, other studies report that precipitation in the TC inner core often surpasses Clausius–Clapeyron expectations[15,16], suggesting a robust enhancement of TC-induced rainfall under warming[13,14,16,17].

Conversely, vertical temperature changes in the troposphere can exert a counteracting effect. Greater warming in the upper troposphere relative to the lower troposphere increases atmospheric stability, weakening the TC secondary circulation and potentially reducing intensity and precipitation[18]. However, when the effects of SST warming, increased atmospheric moisture, and tropospheric stability are considered together, the net response is generally an intensification of TC intensity and precipitation[5,6,13,19].

The shared socioeconomic pathway (SSP) scenarios provide a framework for exploring how factors, such as population growth, economic development, energy use, and policy choices, may influence future climate change and greenhouse gas emissions. The Paris agreement seeks to limit the increase in global mean temperature to well below 2 °C above pre-industrial levels, with efforts to constrain warming to 1.5 °C[20]. In this context, the SSP1-1.9 and SSP1-2.6 scenarios target 1.5 and 2.0 °C warming by 2100, respectively, assuming that net-zero emissions are achieved in the 2050 and 2070s[21]. Examining these scenarios allows an assessment of the potential impacts of a 0.5 °C difference in warming, which can have region- and hazard-specific consequences. While recent studies have investigated the effects of 1.5 and 2.0 °C warming or carbon-neutral scenario on various natural hazards[22–29], relatively few have

[1]Renewable Energy Big Data Laboratory, Korea Institute of Energy Research, Daejeon, South Korea. [2]Division of Environmental Science and Engineering, Pohang University of Science and Technology, Pohang, South Korea. [3]Department of Civil, Urban, Earth, and Environmental Engineering, Ulsan National Institute of Science and Technology, Ulsan, South Korea. ✉e-mail: skmin@postech.ac.kr

focused specifically on tropical cyclone (TC) intensity and precipitation over the WNP.

Despite advances in TC modeling, realistically simulating very intense TCs remains challenging[30,31]. Global climate models often have coarse horizontal resolution, limiting their ability to capture fine-scale TC dynamics. To address this, high-resolution regional climate models have been employed[14,32–34]. For instance, Zhang et al. and Wang et al.[34] reported minimal changes in TC frequency under low-emission scenarios, whereas high-emission scenarios exhibited a substantial decrease. Previous study[14] found that mean precipitation within 500 km of the TC center over land could increase by more than 8% under future warming. However, studies directly comparing TC responses under SSP1-1.9 and SSP1-2.6 over the WNP, particularly using convection-permitting simulations, remain scarce. Previous scenario-comparison studies[35,36] often lacked sufficient resolution to resolve the physical processes and small-scale structures of TCs.

The pseudo-global warming (PGW) method is a widely used dynamic downscaling technique employed to assess the high-resolution impacts of future climate change scenarios. The core principle involves calculating the climate change signal (delta pattern) between the multi-model ensemble mean of a future period and a historical reference period. This calculated delta pattern is added to the initial and boundary conditions of historical reanalysis data (e.g., ERA5 reanalysis) used to drive the regional climate model. Many previous studies have advanced the understanding of future TCs using high-resolution models and the PGW approach[10,37–39]. Previous studies have primarily focused on the magnitude of climate change (e.g., end-of-century impacts under high-emission pathways like SSP5-8.5). However, this study investigates the impact of the emission pathway's speed by comparing two low-emission scenarios (SSP1-1.9 and SSP1-2.6 with net-zero achieved in the 2050 and 2070s, respectively). We demonstrate that the 20-year delay in achieving carbon neutrality (SSP1-2.6 vs. SSP1-1.9) results in a more substantial intensification of WNP TCs, particularly in the expansion of the area affected by extreme winds and precipitation. This specific focus on the differential impact of net-zero timing represents a crucial scientific insight compared to the existing literature.

This study aims to fill this gap by examining the impacts of very low and low emission scenarios (SSP1-1.9 and SSP1-2.6) on TC intensity and precipitation over the WNP using convection-permitting simulations, providing new insights into the sensitivity of TCs to near-term climate mitigation pathways. Our decision to focus on the two lowest emission scenarios is based on the critical need to quantify the physical implications of timely climate mitigation, especially given the impending 1.5 °C global warming threshold. As highlighted by Bevacqua et al.[40], without very stringent climate mitigation, the first year exceeding 1.5 °C warming is highly likely to occur within the 20-year period that will reach an average warming of 1.5 °C. Furthermore, many low-emission scenarios involve a global warming overshoot, where temperatures temporarily exceed the 1.5 °C in the early to mid-21 century[41]. Therefore, our study focuses on these scenarios to evaluate the long-term impact of climate change during the late 21st century.

Results

WRF model evaluation for convection-permitting TC simulations

The weather research and forecasting (WRF) model was configured with a single domain at a convection-permitting horizontal resolution of 3 km, which is essential for accurately representing the TC structure and dynamics, including their intensity and precipitation patterns. The current climate experiment, driven by ERA5 reanalysis data as initial and lateral boundary conditions, is referred to as HIST. Very low and low emission experiments, denoted SSP119 and SSP126, were conducted using a PGW approach, wherein the difference (delta pattern) between CMIP6 SSP1-1.9 (CSSP119), CMIP6 SSP1-2.6 (CSSP126), and CHIST experiments was applied. Refer to "Methods" for details.

Simulated TC tracks, constrained by spectral nudging (see "Methods"), showed no considerable deviation from best track data (Fig. 1a–c). Track errors over time for HIST, SSP119, and SSP126 were generally within 100 km on average, with only a few exceptions throughout the simulation period (Fig. 1d). Comparisons using regional specialized meteorological center (RSMC) and Korea meteorological administration (KMA) best tracks yielded results consistent with those from joint typhoon warning center (JTWC) (Supplementary Fig. 1). Accordingly, differences in TC tracks between experiments were excluded from further analysis.

TC intensity was evaluated using the maximum wind speed simulated by the WRF model (Fig. 1e). Relative to the JTWC best track, the initial 24 h of simulation exhibited minor error; however, the model tended to underestimate TC intensity thereafter. As TCs made landfall and weakened, the intensity error decreased. The cases examined in this study involved extreme-intensity TCs, and underestimation of TC intensity is commonly observed in models, particularly for rapid intensification events, which remain challenging even for convection-permitting simulations[13,42,43]. Extreme TCs often show limited improvement regardless of variations in the physical parameterization schemes chosen[44,45]. To evaluate the precipitation associated with the simulated TCs, we utilized the Integrated Multi-Satellite Retrievals for Global Precipitation Mission (IMERG) final run data as a reference [46]. We assessed the model performance by comparing the area-averaged precipitation within a 500 km radius of the TC center. While individual cases exhibited mixed results, with some TCs showing slight overestimation and others slight underestimation of precipitation, the magnitude of these differences was not large (Fig. 1f). The mean error averaged across all simulated TCs demonstrated that the model's precipitation was reasonably simulated when compared to the IMERG reference data.

Projected changes in tropical cyclone intensity and precipitation under future climates

This study examined changes in the spatial extent of extreme TC intensity under future climate scenarios by analyzing probability density function distributions of maximum wind speed and precipitation (Figs. 2 and 3). In the HIST experiments, the 90th percentile of maximum wind speed and precipitation was approximately 20 m s^{-1} and 30 mm 6 h^{-1}, respectively. Comparisons with future experiments considered both absolute and relative changes. The difference in maximum wind speed between SSP119 and HIST increased toward the extremes, though the trend remained modest. By contrast, SSP126 showed a substantially larger increase. At the 99th percentile, SSP119 exhibited an increase of ~0.4 m s^{-1} (1%) relative to HIST, whereas SSP126 showed an increase of 0.8 m s^{-1} (2%), double that of SSP119. Similar patterns emerged for precipitation, with increases of ~8 mm 6 h^{-1} in SSP119 and ~12 mm 6 h^{-1}. in SSP126 at the 99th percentile. These results indicate a greater expansion of extreme-intensity TC areas in SSP126 than SSP119.

Despite these changes, the relative changes in extreme-intensity areas were generally modest, particularly for SSP119. In SSP126, relative changes in maximum wind speed rose steadily from the 90th to the 100th percentile but plateaued above the 99th percentile. Precipitation increased up to the 95th percentile, after which relative differences remained nearly constant. At the 99th percentile, precipitation increased by ~5% and ~8% for SSP119 and SSP126, respectively. When compared to SST increases in the WNP, these correspond to precipitation increases of ~8% and ~9% per 1 °C warming, slightly exceeding expectations from the Clausius–Clapeyron relation. The scaling rate is estimated based on the ratio of the relative change in precipitation (~5% in SSP119 and ~8% in SSP126) by the magnitude of the SST warming for the WNP basin (~0.6 °C in SSP119 and ~0.9 °C in SSP126). Given the small differences in external forcing between the two scenarios, these results may be subject to uncertainties arising from WRF model physics parameterizations and internal variability. As demonstrated by Nie et al.[47], extreme precipitation events often exhibit a super-Clausius–Clapeyron scaling due to dynamic feedback, where increased moisture convergence and latent heating lead to stronger vertical motion.

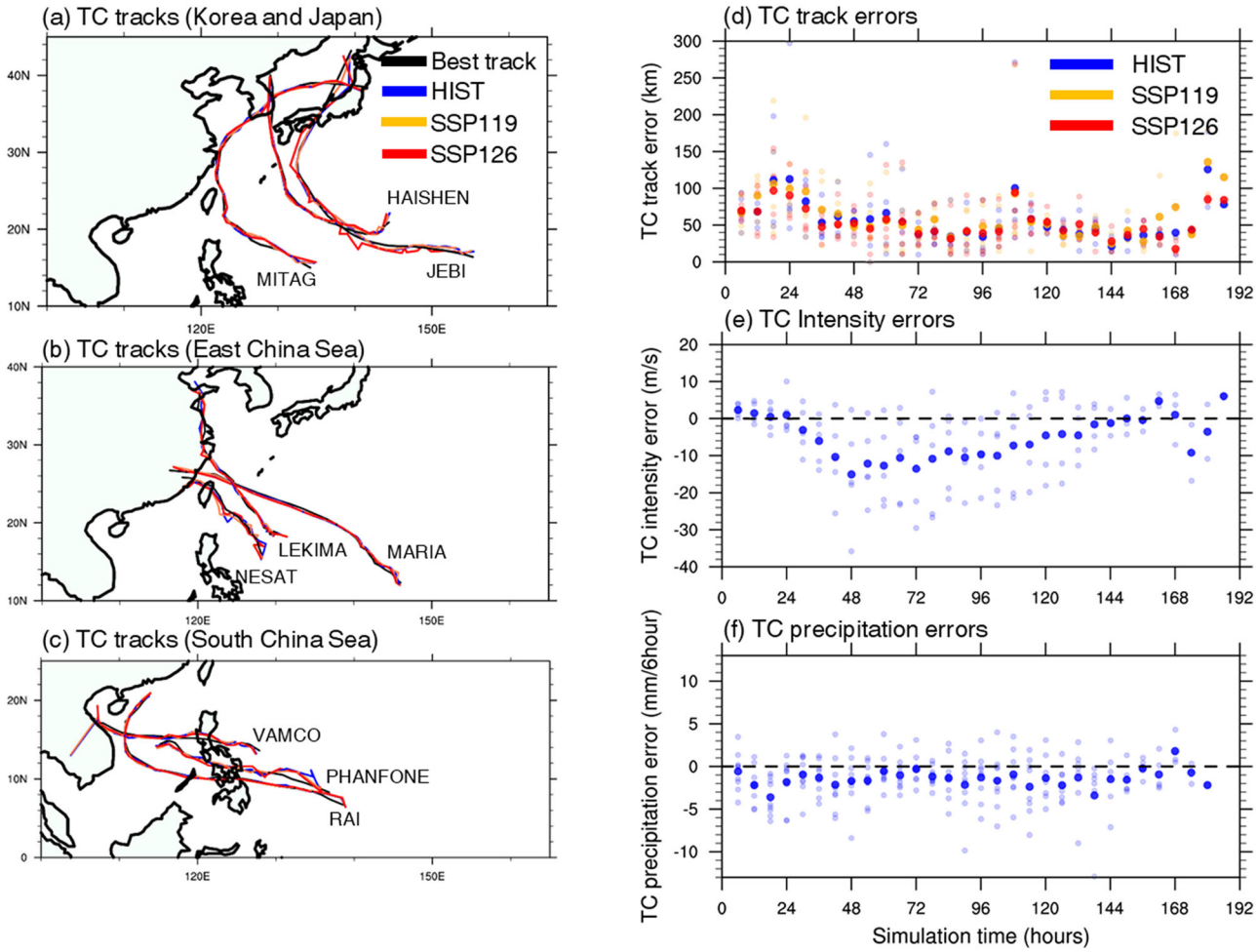

Fig. 1 | Comparison of observed and simulated tropical cyclone tracks, intensity, and precipitation errors. a–c JTWC best track data (black line) and simulated TC tracks (colored lines). **d** TC track errors, **e** intensity errors, and **f** precipitation errors over simulation time. Light circles indicate individual TC cases, and thick circles represent the mean across all experiments at each simulation time.

The results of this study confirm that the intensity of extreme TC values increases under future climate experiments. Furthermore, by identifying regions exceeding specific thresholds, we quantitatively and spatially analyzed changes in extreme-intensity areas (Fig. 4). Three thresholds were applied for both maximum wind speed and precipitation, and the number of grid points exceeding these thresholds was counted to assess their spatial distribution (Supplementary Figs. 2 and 3). In HIST, grids with wind speeds exceeding 30 m s^{-1} were concentrated within a 50 km radius of the TC center (Fig. 4a), with the highest counts occurring near the eyewall for other thresholds as well (Supplementary Fig. 2). Differences in extreme wind areas between SSP experiments and HIST were modest at the 20 and 30 m s^{-1} thresholds (Fig. 4i). However, at the extreme threshold of 40 m s^{-1}, SSP126 showed an area increase exceeding 20% relative to HIST, whereas SSP119 increased by more than 13%. Substantial differences between SSP experiments were observed only at the 40 m s^{-1} threshold, with similar patterns for other thresholds.

Precipitation exhibited larger area increases compared to maximum wind speed (Fig. 4 and Supplementary Fig. 3). At the 100 mm 6 h^{-1} threshold, areas of heavy precipitation increased by approximately 15% and 22% for SSP119 and SSP126, respectively, relative to HIST. At the 150 mm 6 h^{-1} threshold, increases reached 20% and 30%, respectively. Between future experiments, SSP126 showed 5–10% larger area increases than SSP119 at both thresholds. As for the TC size, we calculated the radius of 50-kt winds (R50) to represent the size of each simulated TC. The result shows that the differences in TC size vary considerably depending on the specific case and the simulation time step (Supplementary Fig. 4). Overall, the SSP scenarios generally exhibit a slightly larger TC size compared to the HIST experiment. However, the difference in R50 between the two SSP scenarios (SSP126 minus SSP119) was found to be minimal.

We conducted an additional analysis specifically focusing on the evolution of TCs during the landfall phase. We defined the landfall period as the duration from the moment the land first appears within a 500 km radius of the TC center until the end of the simulation. Considering that intensity typically weakens as the TC approaches land, we adjusted the intensity thresholds for the spatial distribution analysis to be lower than those used in Fig. 4. The spatial distribution results show that both wind speed and precipitation intensity increase in the SSP experiments compared to the HIST experiment (Fig. 5). The rate of increase in the affected area is more pronounced at higher thresholds, indicating a substantial shift toward more extreme events, which is similar result compared with Figs. 4 and 5i, j). When comparing the SSP experiments, the change rate of intensity during the landfall period showed a slight decrease compared to the analysis that included the entire simulation period. These results indicate that maximum wind speed and heavy precipitation from TCs are projected to intensify under a warmer climate, particularly in extreme-intensity regions, suggesting that potential damage from TCs could increase in the future.

Key factors contributing to future TC intensification

To identify the drivers of TC intensification in warmer climates, particularly under extreme conditions, we analyzed key environmental variables closely

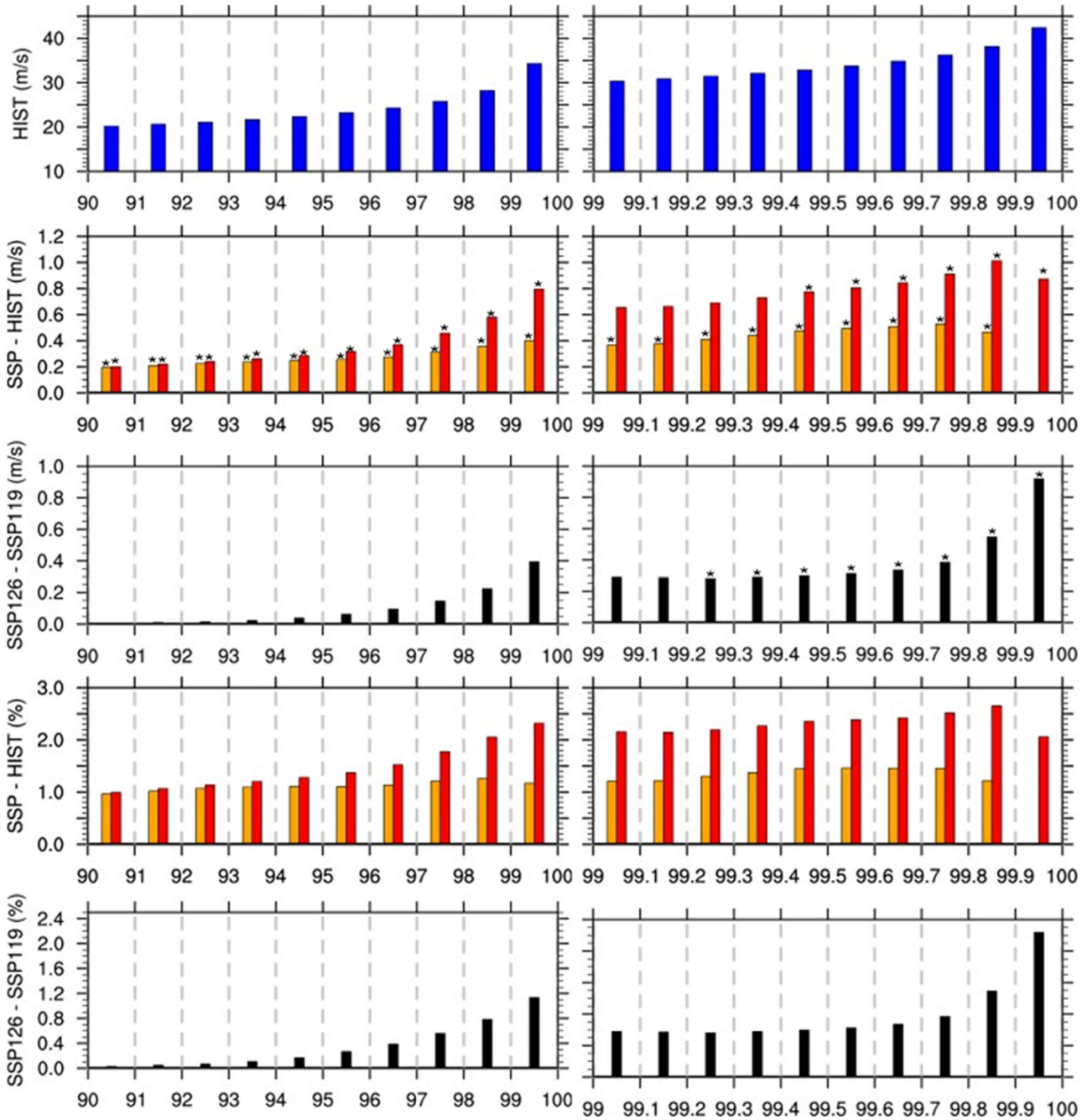

Fig. 2 | Probability distribution and changes in extreme maximum wind speeds across scenarios. Probability distribution of extreme maximum wind speeds (90th–100th percentiles). Blue bars represent HIST, while orange and red bars denote differences from HIST for SSP119 and SSP126, respectively. Black bars show the difference between future experiments (SSP126–SSP119). The second and third rows indicate absolute changes (m s^{-1}) and the fourth and fifth rows show relative changes (%). Asterisks indicate regions where the sign of the difference is consistent across at least seven out of the nine simulated TC cases. Asterisks are included only in the absolute difference plots.

linked to TC intensity, namely water vapor and vertical motion (omega; Fig. 6). Previous studies have shown that abundant water vapor and strong vertical ascent favor TC intensification[48–50]. Both variables were examined within a 500 km radius of the TC center, using vertical cross-sections to compare differences across experiments (Fig. 6a–h).

Water vapor, strongly governed by temperature, is concentrated near the surface and decreases with altitude. Warmer SST and near-surface air temperatures increase the saturation vapor pressure, leading to a higher supply of moisture for the TC (following the Clausius–Clapeyron relationship). This provides more latent heat for intensification. Enhanced latent heat release leads to a stronger thermal gradient, which intensifies the inflow and vertical motion near the eyewall. This strengthens the TC's secondary circulation, efficiently converging more moisture into the inner core, thus causing positive feedback that intensifies both wind speed and precipitation. Differences between the two SSP scenarios were apparent, with SSP126 simulating a more humid environment than SSP119. Vertical motion, most pronounced near the TC eyewall, drives intense precipitation and is thus a crucial factor for TC intensification. Strong ascent developed within ~200 km of the TC center, with weaker signals at greater distances. SSP119 simulated somewhat stronger vertical motion than HIST but over a limited region, whereas SSP126 produced widespread intensification of vertical ascent within 200 km, supporting enhanced TC precipitation.

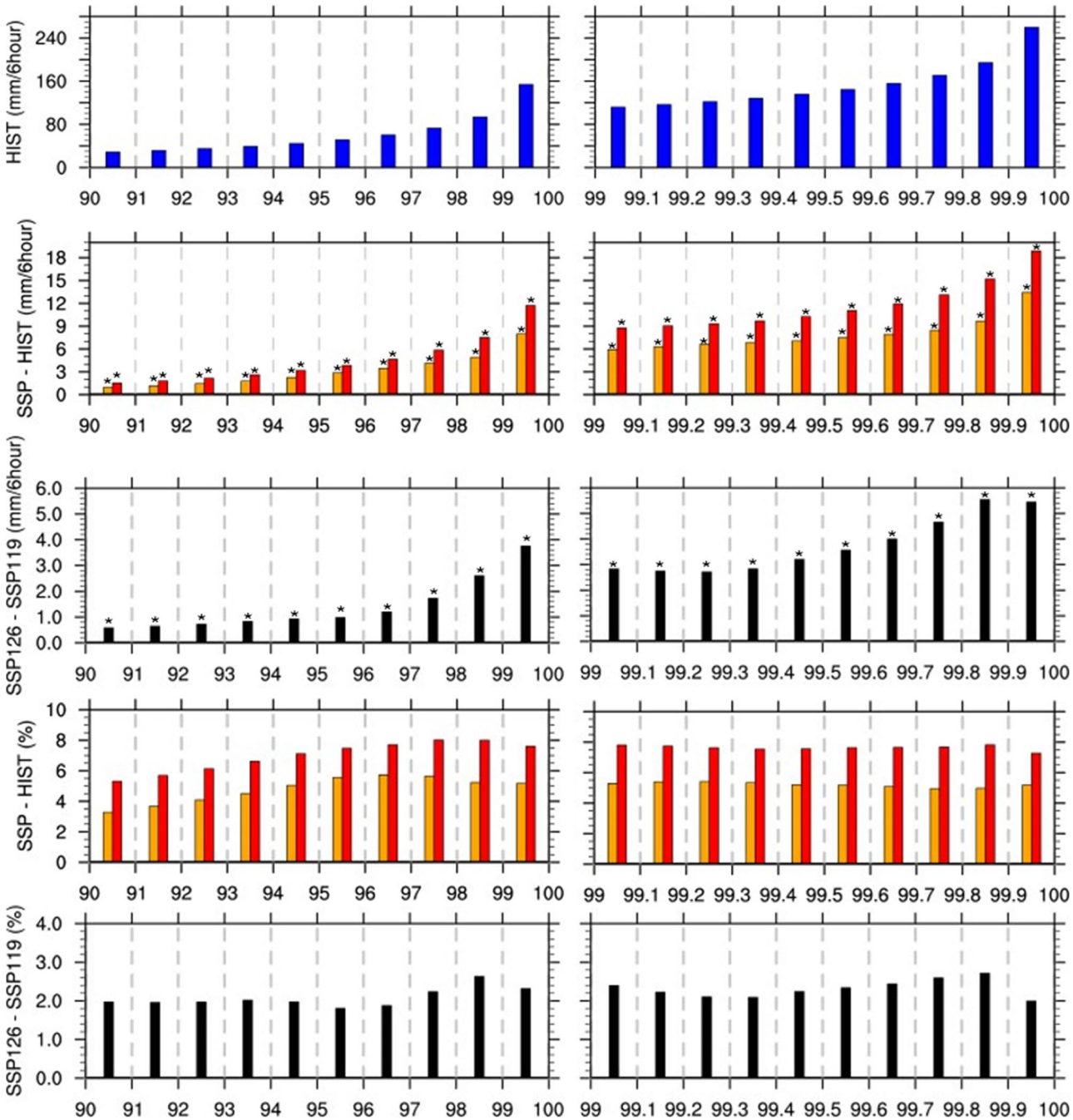

Fig. 3 | Probability distribution and changes in extreme precipitation across scenarios. Same as Fig. 2, but for precipitation.

To quantify the role of water vapor and vertical motion in modulating TC wind speed and precipitation, we examined inter-case correlations across all simulations. For each TC case, differences in wind speed, precipitation, water vapor, and vertical motion between future and current climates were assessed. Vertically integrated water vapor (1000–200 hPa, 500 km radius; Fig. 6i, k) showed a positive correlation with wind speed, though not statistically significant. By contrast, precipitation differences were strongly correlated with water vapor ($r = 0.77$), indicating that moisture directly influences rainfall but only indirectly affects wind intensity. Vertical motion, averaged between 1000 and 200 hPa within 200 km, exhibited stronger correlations with both wind speed ($r = -0.59$) and precipitation ($r = -0.64$). This reflects the closer link between TC secondary circulation and dynamic intensification. Nevertheless, several cases showed weaker or negligible changes in vertical motion, highlighting uncertainties in dynamic responses[51].

To quantify the relative influence of these factors, we calculated the coefficient of determination (R^2) by squaring the correlation coefficients between precipitation change and each driver. The results indicate that the thermodynamic factor, represented by the change in water vapor, accounts for approximately 59% ($R^2 = 0.59$) of the total variance in the precipitation response, while the dynamic factor, represented by vertical motion, explains about 41% ($R^2 = 0.41$). Furthermore, we investigated the relationship between these two drivers and found that the correlation between water vapor changes and vertical motion changes is not statistically significant. This lack of correlation indicates that the thermodynamic and dynamic mechanisms act as independent controls on the precipitation increases. We have performed an additional analysis of the vertical structure of the tangential and radial winds for the SSP scenarios compared to the HIST experiment. Our results show that the SSP experiments simulate stronger

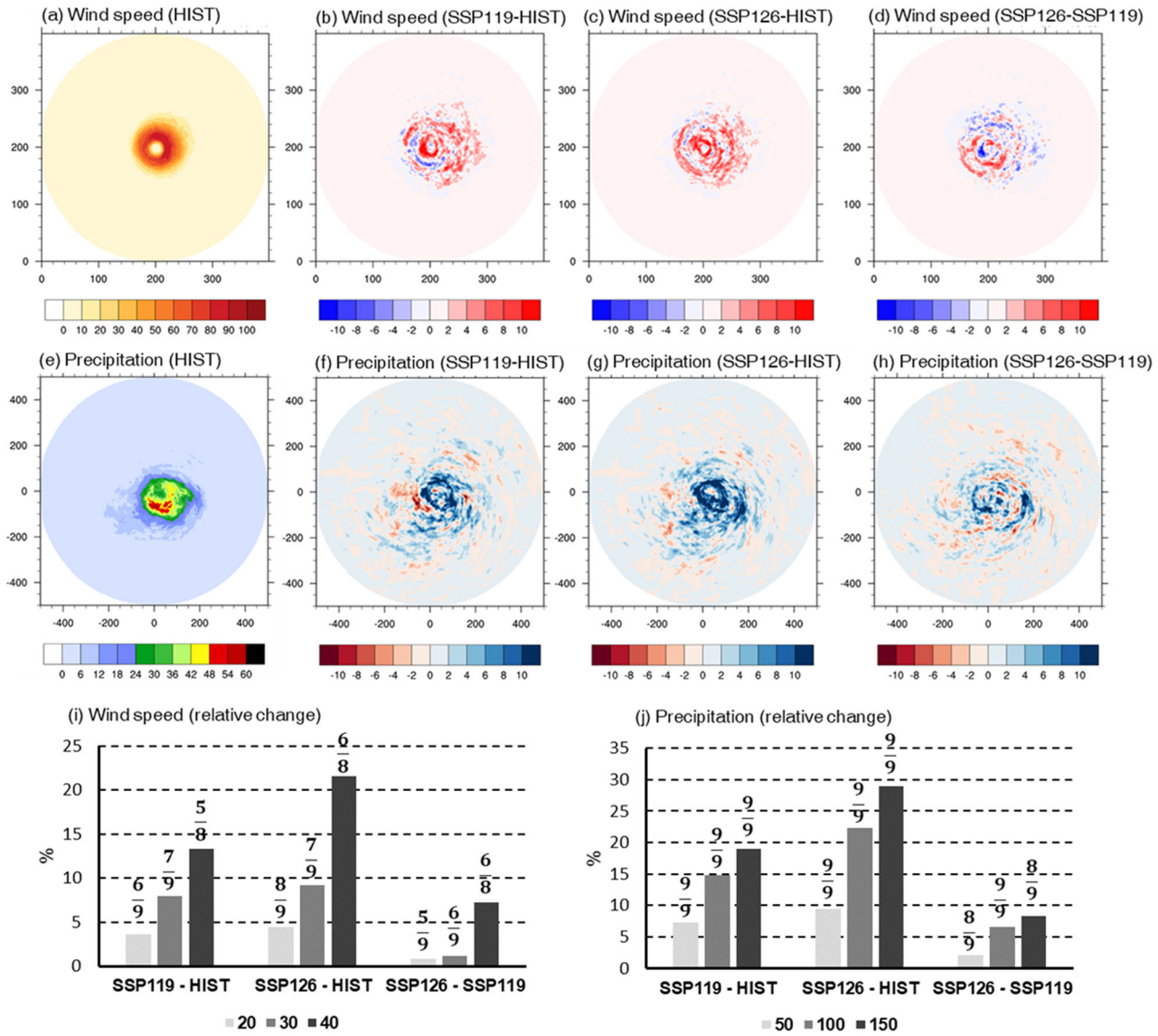

Fig. 4 | Spatial distribution and relative changes in frequency for extreme wind speed and precipitation. Distribution of number of grids exceeding thresholds of 30 m s^{-1} for maximum wind speed (**a**–**d**) and 100 mm 6 h^{-1} for precipitation (**e**–**h**). The first column shows HIST, while the remaining columns indicate differences among the experiments. **i**, **j** Present relative changes in the number of grids exceeding three thresholds for wind (20, 30, and 40 m s^{-1}) and precipitation (50, 100, and 150 mm 6 h^{-1}), respectively. Fractions displayed above **i**, **j** denote the proportion of TC cases with positive differences relative to the total number of cases.

tangential and radial winds throughout the vertical column than the HIST experiment (Supplementary Fig. 5). The enhanced radial inflow in the lower levels and outflow in the upper levels, combined with the intensified tangential circulation, represent a more robust TC structure. These enhancements provide the physical foundation for the stronger maximum wind speeds and the precipitation in the future scenarios.

Overall, these convection-permitting simulations suggest that TCs over the WNP are likely to intensify and produce more damaging impacts in a warmer climate. Moreover, intensification is projected to be more severe under the low emission pathway (SSP1-2.6) than under the very-low emission pathway (SSP1-1.9).

Conclusions

In this study, we investigated changes in TC activity under very low- and low-emission scenarios (SSP1-1.9 and SSP1-2.6, respectively). Using the convection-permitting WRF model, we assessed the potential impacts of 1.5 and 2 °C warming on TC intensity and precipitation over the WNP. Although the 3 km resolution enabled more realistic representation of TC structure, limitations remained in capturing rapid intensification. Nonetheless, the application of spectral nudging effectively minimized track error across all experiments. This was critical because it allowed us to isolate the influence of thermodynamic factors (temperature and humidity changes) while reducing the confounding effect of track changes.

The differences in TC wind and precipitation between future and present climates were most pronounced at extreme thresholds. While changes in weaker wind and rainfall were modest, substantial increases emerged in extreme conditions. For example, grid areas exceeding 40 m s^{-1} expanded by ~13% and 22% in SSP1-1.9 and SSP1-2.6, respectively. For precipitation above 150 mm 6 h^{-1}, the corresponding increases were ~19 and 29%. These enhancements in extreme wind and rainfall were strongly associated with elevated atmospheric moisture and intensified vertical motion under warmer climates, as supported by inter-experiment correlations. Our results thus provide a quantitative assessment of how TC intensity and precipitation may evolve in the WNP under near-future low-emission scenarios. If warming exceeds these levels, future TCs could become even more destructive.

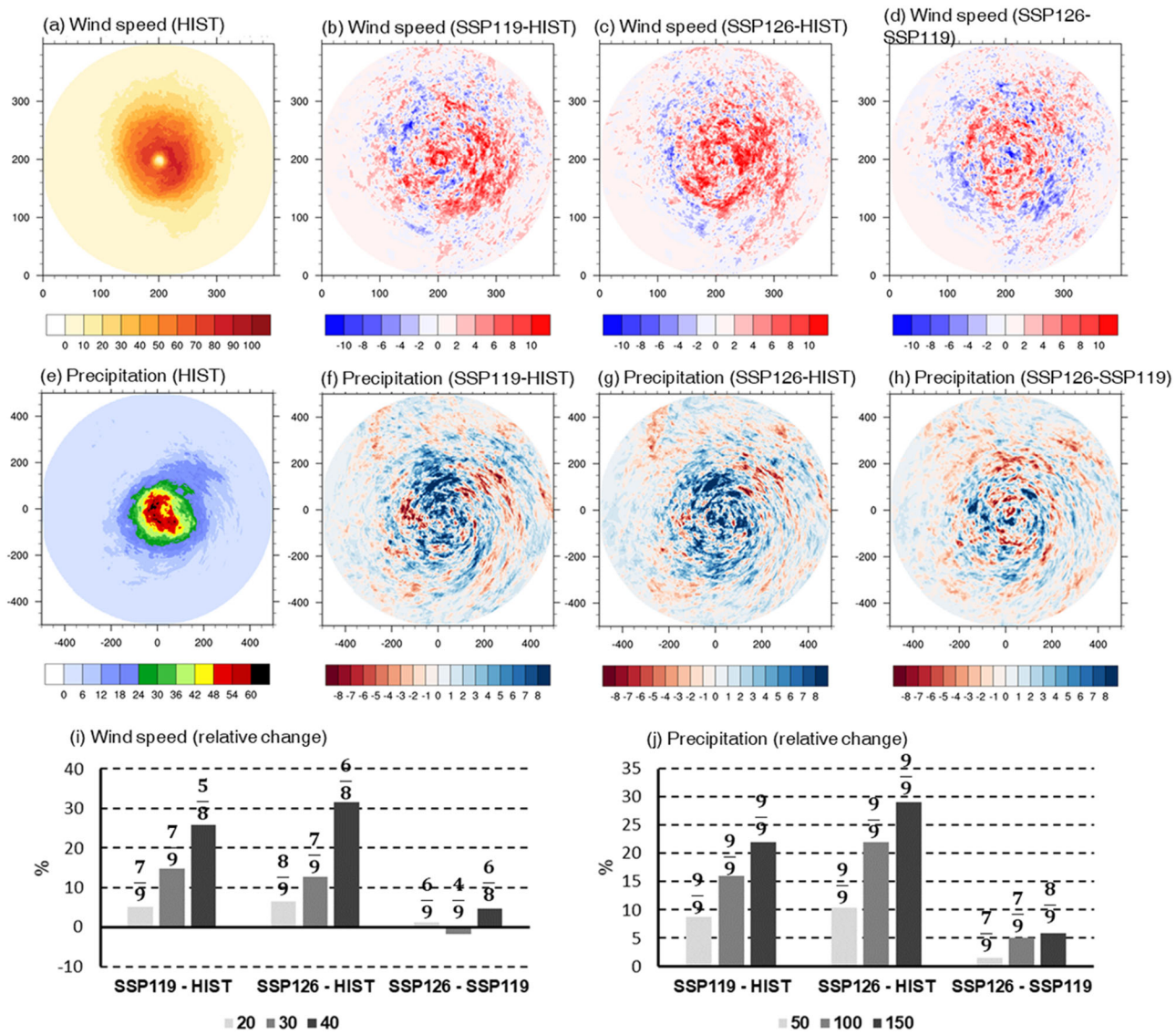

Fig. 5 | Spatial distribution and relative changes in frequency for extreme wind speed and precipitation during landfall period. Distribution of number of grids exceeding thresholds of 20 m s^{-1} for maximum wind speed (**a**–**d**) and 50 mm 6 h^{-1} for precipitation (**e**–**h**). The first column shows HIST, while the remaining columns indicate differences among the experiments. **i**, **j** Present relative changes in the number of grids exceeding three thresholds for wind (20, 30, and 40 m s^{-1}) and precipitation (50, 100, and 150 mm 6 h^{-1}), respectively. Fractions displayed above **i**, **j** denote the proportion of TC cases with positive differences relative to the total number of cases. The analysis was conducted specifically for the landfall period.

These findings are broadly consistent with previous studies on TC activity under SSP1-1.9 and SSP1-2.6 scenarios[35,36,52]. For instance, Wehner et al.[35] projected an increase in category 4–5 TCs and a decrease in weaker storms globally using a high-resolution (0.25°) model. Wen et al.[36] estimated that TC-related economic losses would increase four- and seven-fold under 1.5 and 2 °C warming, respectively, based on regional simulations at 0.5° resolution. However, such global or low-resolution regional models cannot fully capture small-scale processes critical for TC intensity and precipitation. The novelty of our study lies in the use of convection-permitting simulations specifically for the WNP, one of the most TC-active basins, enabling improved representation of storm dynamics under low-emission scenarios. The use of a large, single convection-permitting domain to directly downscale climate signals has been successfully adopted in many previous PGW studies investigating TCs[10,13,37,53]. Some studies[13,37] have shown that high-resolution results, particularly for consistent signals, such as intensity increases under high-emission scenarios, are often comparable whether a nested or a single-domain approach is employed. Furthermore, due to the large size and diverse tracks of the selected TCs over the WNP, a single and large domain was necessary to encompass the entire life cycle of each TC. For WNP TCs, the dynamics of the WNP subtropical high (WNPSH) are important. By selecting a sufficiently large 3 km domain, we ensured that the key large-scale environment influencing TC steering and intensification (including the WNPSH) was simulated at the high, convection-permitting resolution, even at the cost of higher computational resources.

It should be emphasized that our experiments considered only nine strongly landfalling TCs. As such, the simulated changes are most applicable to intense events, and the response of weaker TCs remains uncertain. The sensitivity of currently weak TCs to future warming may differ substantially, and their potential to intensify could present substantial risks. Further work is needed to evaluate a wider range of TC intensities. Furthermore, the systematic underestimation of TC intensity in the HIST suggests that our model may struggle to fully capture the maximum wind speeds during the rapid intensification phase. Nevertheless, simulated TC cases showed a consistent signal. This consistent signal in SSP experiments remains even when analyzing the extreme intensity range (Fig. 4). We found that the spread among the GCM ensemble members is

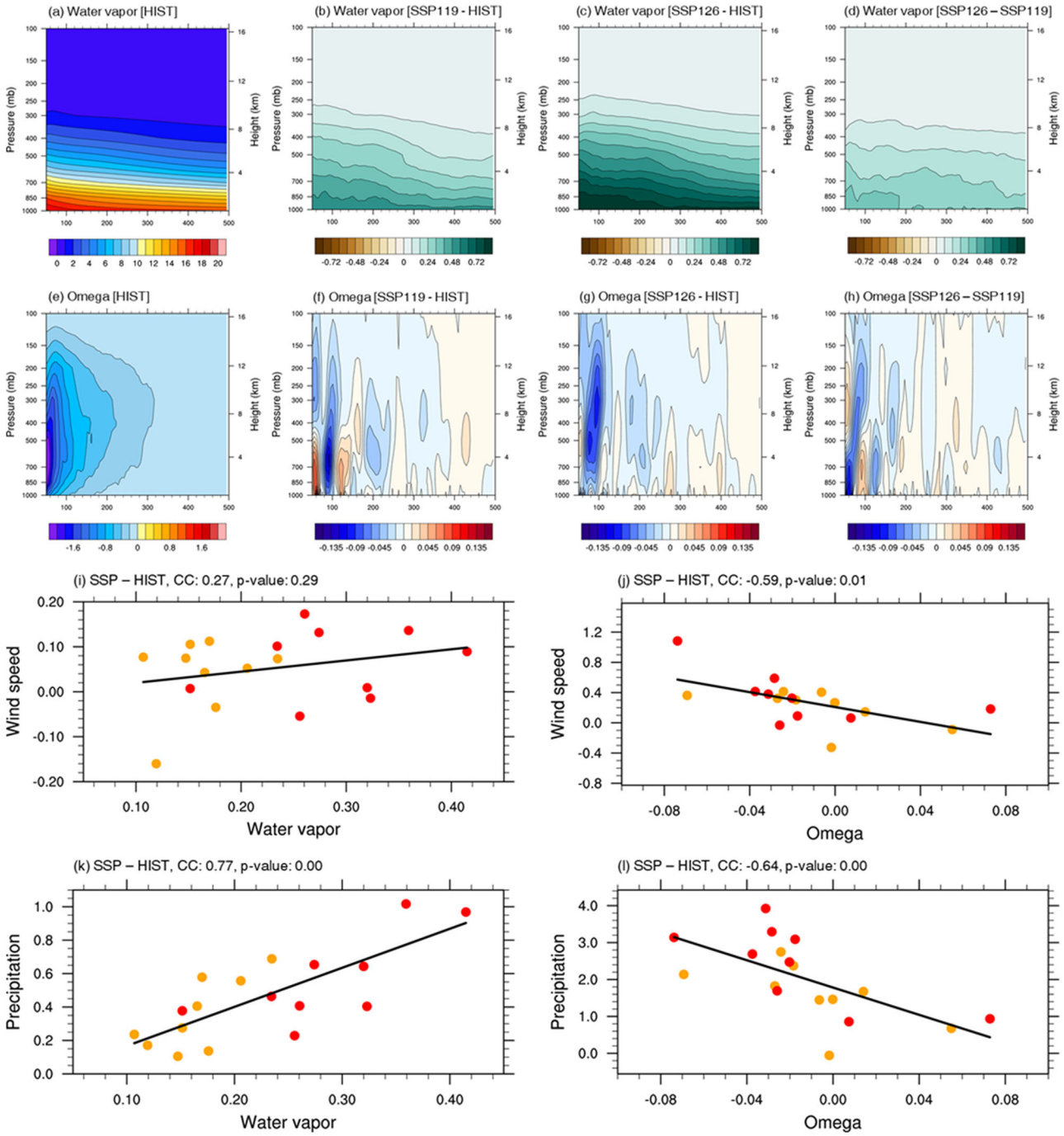

Fig. 6 | Differences in environmental drivers within a 500 km radius and their relationships with tropical cyclone wind speed and precipitation. Differences in **a**–**d** water vapor (g kg^{-1}) and **e**–**h** omega (hPa s^{-1}) within a 500 km radius between experiments. Scatterplots of differences in **i** wind speed and **k** precipitation versus vertically integrated water vapor within 500 km, and in **j** wind speed and **l** precipitation versus vertically averaged omega within 200 km. Orange and red markers denote SSP119 and SSP126, respectively. Correlation coefficients (CC) and *p*-values are indicated.

quite large, and this difference is substantially greater than the difference between the SSP scenarios (Supplementary Fig. 6). While the high uncertainty among GCMs represents a considerable limitation of this study, we attempted to mitigate this by utilizing a large number of GCMs. Furthermore, because the inter-model spreads remain relatively small in the scenario difference (SSP126–SSP119), we believe that the delta calculation itself remains reliable.

Due to the demanding large computational resources, conducting additional physics sensitivity tests was beyond the scope of this study. Instead, we ensured the reliability of our findings by using physical parameterization schemes validated as optimal for TC simulations in previous studies. Park et al.[54] have demonstrated the superior performance of the WSM6 scheme in predicting the track and intensity of WNP TCs. Also, the YSU scheme was chosen because it has been shown to realistically simulate TC intensity compared to other PBL schemes[55]. We also did not incorporate dynamic ocean-atmosphere feedbacks, such as oceanic cooling (the cold wake) or wave-current interactions, in our simulations. Performing fully coupled ocean-atmosphere simulations for our experimental design would have been computationally prohibitive and exceeded the scope of this study.

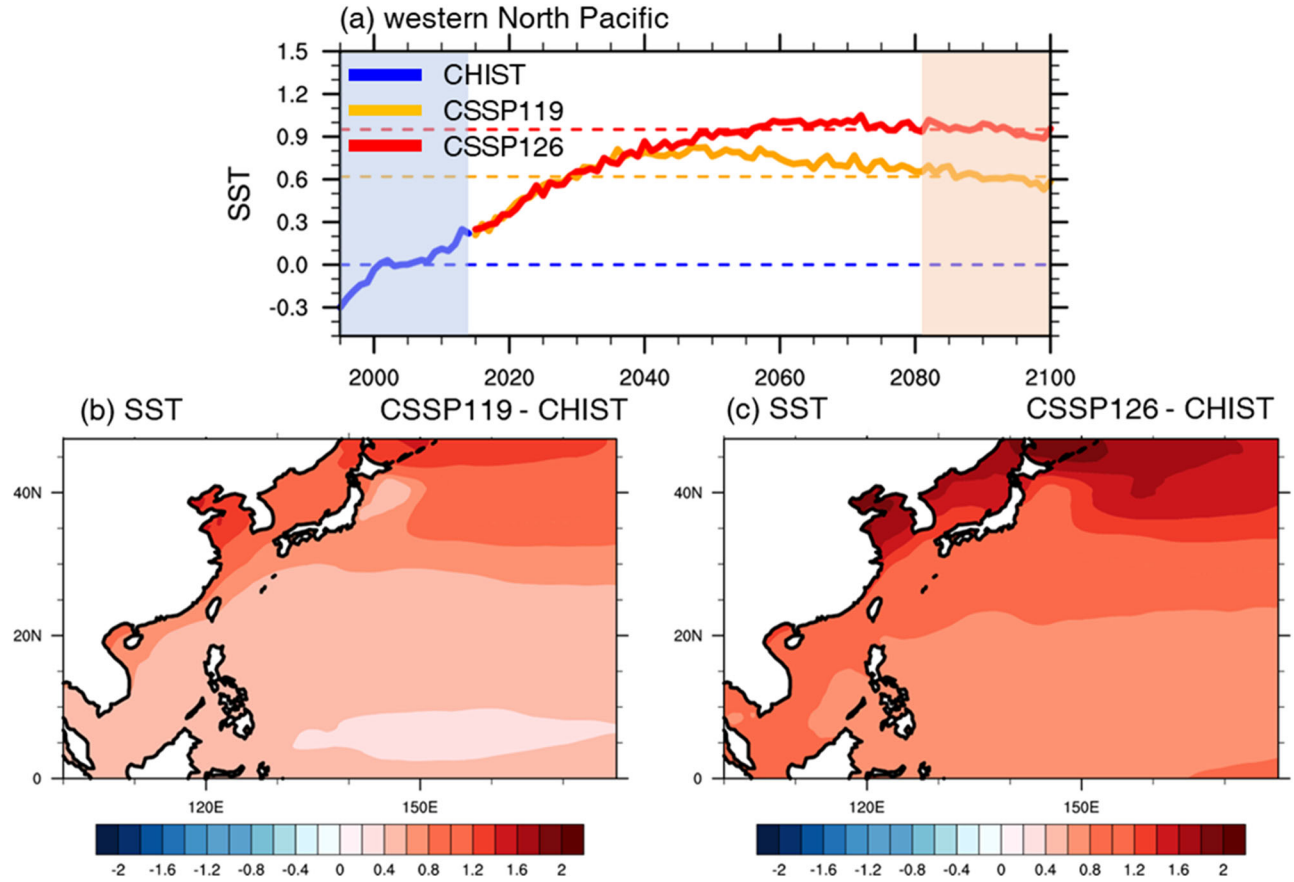

Fig. 7 | Temporal and spatial variations of sea surface temperature in the western North Pacific. a Time series of sea surface temperature (SST) changes in the WNP for each experiment. The y-axis is referenced to the 20-year average of the historical experiment (1995–2014). Blue and orange shading denote the historical (1995–2014) and future (2081–2100) 20-year periods, respectively. Dashed lines indicate the 20-year mean SST for each experiment. Spatial distributions of SST differences over the WNP between future and present periods are shown for **b** CSSP119 and **c** CSSP126.

In conclusion, our study provides additional evidence that global warming substantially intensifies TC wind and precipitation, even under scenarios assuming carbon neutrality by mid-to-late 21st century. Notably, stronger TCs were projected in both SSP1-1.9 and SSP1-2.6, despite their differences in the timing of net-zero emissions. These results underscore the urgency of limiting global warming to reduce future TC risks and highlight the importance of sustained research to inform policy and disaster preparedness in a warming world.

Methods

Data and model configuration

To evaluate whether the model reasonably reproduced TC tracks and intensity, best track datasets from the JTWC, RSMC, and KMA were used for validation. TC activity under global warming over the WNP was simulated with the WRF model version 4.0, which has been widely applied in both short-term forcast[56–59] and long-term climate simulations[60,61].

The ERA5 reanalysis dataset[62], produced by the European Center for Medium-Range Weather Forecasts, was used as initial and lateral boundary conditions. ERA5 provides global coverage with ~31 km horizontal resolution. Daily optimum interpolation sea surface temperature (OISST) data (0.25° resolution) were prescribed as lower boundary conditions. For evaluating precipitation induced by TCs, the IMERG Final Run dataset was employed.

The WRF model employed a single domain at a convection-permitting horizontal resolution of 3 km, following configurations similar to Lee et al.[42]. The domain comprised 1801 × 2001 grid points in the horizontal and 50 vertical levels. Physical parameterizations included the WRF single-moment 6-class microphysics (WSM6) cloud microphysics scheme[63], rapid radiative transfer model for general circulation model (RRTMG) for both shortwave and longwave radiation[64], and Yonsei University (YSU) planetary boundary layer scheme[65]. The cumulus parameterization was deactivated owing to the convection-permitting resolution.

Spectral nudging[66,67] was applied to reduce track deviations among experiments, a technique widely used in previous TC studies[10,43,68,69]. To preserve TC dynamics, nudging was not applied in the lower troposphere[70], and was linearly increased from zero at the 10th sigma level to the model top. The spectral nudging was applied using a sufficiently large wavelength (approximately 1500 km). This large wavelength ensures that only the coarse synoptic-scale features are constrained. Therefore, minimizing any dynamical influence on the TC-scale circulation. Huang et al.[71]. Accurate simulation of TC tracks is essential for assessing the impacts of global warming on TC intensity and precipitation, and the spectral nudging approach ensured consistent storm trajectories across experiments. Furthermore, Huang et al.[71] and Moon et al.[70] described that the application of spectral nudging led to improved TC intensity, indicating that spectral nudging can often help maintain realistic large-scale environmental conditions.

Experimental design

Extremely intense TCs over the WNP during 2017–2021 were selected based on the following criteria:

- TCs reached tropical storm (TS; 17 m s^{-1} ≤ maximum wind speed < 32 m s^{-1}) or higher intensity and persisted for 4–8 days.
- TCs exhibited a landfall intensity ≥ 41 m s^{-1} (80 knots).
- TCs occurring in the South China Sea were excluded.

Cases lasting at least 4 days at TS intensity or higher were chosen to adequately capture the influence of warming on TC behavior. Due to computational constraints associated with single-domain convection-permitting simulations, only cases with simulation periods shorter than 8 days were selected. TCs occurring in the South China Sea were excluded from the case selection since their TC track sometimes exceeded the boundaries of the simulation domain. The simulation start time was set when the TC intensified from tropical depression (TD; maximum wind speed $\leq 17\ m\ s^{-1}$) to TS, and the end time corresponded to the point when the TC weakened back to TS. Using these criteria, nine TC cases were selected; detailed information for each case is provided in Supplementary Table 1.

Future changes in SST and atmospheric conditions were estimated using general circulation models (GCMs) included in the Coupled Model Intercomparison Project phase 6 (CMIP6)[72]. SSP scenarios, which incorporate potential future socioeconomic pathways, were applied[73]. The CMIP6 models used are summarized in the Supplementary Table 2. Based on the multi-model ensemble mean (using 9 GCMs), we computed delta patterns representing changes in SST, atmospheric temperature, and relative humidity. The CMIP6 historical experiment (CHIST), representing the current climate, was defined over 1995–2014 (blue shading in Fig. 7a). The projected SST increases over the WNP in CSSP119 and CSSP126 were approximately 0.6 and 0.9 °C relative to the CHIST. Warming was stronger in the mid-latitude and weaker near the equator, with CSSP126 exhibiting slightly higher warming than CSSP119; spatial patterns were broadly similar (Fig. 7b, c).

This study employed the PGW approach, a widely used method to assess the impacts of future climate change[74–77]. The PGW method modifies the initial and boundary conditions of regional climate models based on projected thermodynamic changes, enabling evaluation of how extreme events may evolve under future climates[13,78]. Following previous studies, monthly SST, atmospheric temperature, and relative humidity were adjusted to reflect thermodynamic changes[5,79,80]. The horizontal wind fields were not altered to maintain consistent TC tracks; previous work suggests that modifying horizontal winds has minimal influence on TC intensity[13]. We also did not adjust the geopotential height and pressure fields. While we rely on the WRF model's core dynamics to achieve a new hydrostatic equilibrium internally. Including dynamically consistent geopotential and pressure would ensure near-perfect hydrostatic consistency at the initial time step and along the lateral boundaries. However, for mature TCs, the maximum intensity and inner core structure are primarily controlled by convection physics and enhanced thermodynamic forcing (moisture and SST fluxes) within the inner core. Adjusting GCM-derived perturbations to geopotential height and pressure directly influences the large-scale steering flow. This application would change the simulated TC track for the future compared to the historical track. Furthermore, the recomputed geopotential height field in the WRF preprocessing system (WPS) is hydrostatically balanced, and any imbalance between the wind and mass fields is sufficiently small[81].

Data availability

The data used in this study are available as follows: JTWC best track data (https://www.metoc.navy.mil/jtwc/jtwc.html), RSMC best track data (https://www.jma.go.jp/jma/jma-eng/jma-center/rsmc-hp-pub-eg/besttrack.html), KMA best track data (https://www.weather.go.kr/w/typhoon/typ-history.do), ERA5, OISST (https://psl.noaa.gov/data/gridded/data.noaa.oisst.v2.highres. html), and CMIP6 GCMs (https://esgf-node.ipsl.upmc.fr/projects/cmip6-ipsl/), IMERG Final Run (https://gpm.nasa.gov/). WRF simulation datasets that support the results can be found in the repository on Zenodo (https://doi.org/10.5281/zenodo.18399115).

Code availability

The weather research and forecasting (WRF) model used in this study is an open-source software available at https://github.com/wrf-model/WRF/releases. This research specifically utilized the WRF model version 4.0. The visualization of the simulation results was performed using NCAR Command Language (NCL). Representative scripts for analyzing TC intensity and plotting TC tracks are publicly available on Zenodo at https://doi.org/10.5281/zenodo.18384153 and https://doi.org/10.5281/zenodo.18384198. Other analysis codes used in this study are available from the corresponding author upon reasonable request.

Received: 26 September 2025; Accepted: 10 February 2026;
Published online: 25 February 2026

References

1. Balaguru, K., Foltz, G. R., Leung, L. R. & Emanuel, K. A. Global warming-induced upper-ocean freshening and the intensification of super typhoons. *Nat. Commun.* **7**, 13670 (2016).
2. Gray, W. M. Global view of the origin of tropical disturbances and storms. *Mon. Weather Rev.* **96**, 669–700 (1968).
3. Patricola, C. M., Cassidy, D. J. & Klotzbach, P. J. Tropical oceanic influences on observed global tropical cyclone frequency. *Geophys. Res. Lett.* **49**, e2022GL099354 (2022).
4. Peduzzi, P. et al. Global trends in tropical cyclone risk. *Nat. Clim. Change* **2**, 289–294 (2012).
5. Nakamura, R., Shibayama, T., Esteban, M. & Iwamoto, T. Future typhoon and storm surges under different global warming scenarios: case study of typhoon Haiyan (2013). *Nat. Hazards* **82**, 1645–1681 (2016).
6. Wang, S. S., Zhao, L., Yoon, J.-H., Klotzbach, P. & Gillies, R. R. Quantitative attribution of climate effects on Hurricane Harvey's extreme rainfall in Texas. *Environ. Res. Lett.* **13**, 054014 (2018).
7. Allen, M. R. & Ingram, W. J. Constraints on future changes in climate and the hydrologic cycle. *Nature* **419**, 224–232 (2002).
8. Held, I. M. & Soden, B. J. Robust responses of the hydrological cycle to global warming. *J. Clim.* **19**, 5686–5699 (2006).
9. Panthou, G., Mailhot, A., Laurence, E. & Talbot, G. Relationship between surface temperature and extreme rainfalls: a multi-time-scale and event-based analysis. *J. Hydrometeorol.* **15**, 1999–2011 (2014).
10. Gutmann, E. D. et al. Changes in hurricanes from a 13-yr convection-permitting pseudo–global warming simulation. *J. Clim.* **31**, 3643–3657 (2018).
11. Hallam, S. et al. The relationship between sea surface temperature anomalies, wind and translation speed and North Atlantic tropical cyclone rainfall over ocean and land. *Environ. Res. Commun.* **5**, 025007 (2023).
12. Kim, H.-S. et al. Tropical cyclone simulation and response to CO_2 doubling in the GFDL CM2. 5 high-resolution coupled climate model. *J. Clim.* **27**, 8034–8054 (2014).
13. Patricola, C. M. & Wehner, M. F. Anthropogenic influences on major tropical cyclone events. *Nature* **563**, 339–346 (2018).
14. Wright, D. B., Knutson, T. R. & Smith, J. A. Regional climate model projections of rainfall from US landfalling tropical cyclones. *Clim. Dyn.* **45**, 3365–3379 (2015).
15. Knutson, T. R. et al. Global projections of intense tropical cyclone activity for the late twenty-first century from dynamical downscaling of CMIP5/RCP4.5 scenarios. *J. Clim.* **28**, 7203–7224 (2015).
16. Liu, M., Vecchi, G. A., Smith, J. A. & Knutson, T. R. Causes of large projected increases in hurricane precipitation rates with global warming. *NPJ Clim. Atmos. Sci.* **2**, 38 (2019).
17. Stansfield, A. M. & Reed, K. A. Global tropical cyclone precipitation scaling with sea surface temperature. *NPJ Clim. Atmos. Sci.* **6**, 60 (2023).
18. Liu, M., Yang, L., Smith, J. A. & Vecchi, G. A. Response of extreme rainfall for landfalling tropical cyclones undergoing extratropical transition to projected climate change: Hurricane Irene (2011). *Earth's Future* **8**, e2019EF001360 (2020).
19. Sobel, A. H. et al. Human influence on tropical cyclone intensity. *Science* **353**, 242–246 (2016).

20. Agreement, P. in report of the conference of the parties to the United Nations framework convention on climate change (21st session, 2015: Paris). Retrived December (Vol. 4, No. 2017, p. 2). Getzville, NY, USA: HeinOnline (2015, December).
21. Tebaldi, C. et al. Climate model projections from the scenario model intercomparison project (ScenarioMIP) of CMIP6. *Earth Syst. Dyn.* **12**, 253–293 (2021).
22. Ali, H. & Mishra, V. Increase in subdaily precipitation extremes in India under 1.5 and 2.0 °C warming worlds. *Geophys. Res. Lett.* **45**, 6972–6982 (2018).
23. Iyakaremye, V., Zeng, G. & Zhang, G. Changes in extreme temperature events over Africa under 1.5 and 2.0 °C global warming scenarios. *Int. J. Climatol.* **41**, 1506–1524 (2021).
24. Karmalkar, A. V. & Bradley, R. S. Consequences of global warming of 1.5 °C and 2 °C for regional temperature and precipitation changes in the contiguous United States. *PLoS ONE* **12**, e0168697 (2017).
25. Shi, C., Jiang, Z.-H., Chen, W.-L. & Li, L. Changes in temperature extremes over China under 1.5 °C and 2 °C global warming targets. *Adv. Clim. Change Res.* **9**, 120–129 (2018).
26. Shi, X. et al. Impacts and socioeconomic exposures of global extreme precipitation events in 1.5 and 2.0 °C warmer climates. *Sci. Total Environ.* **766**, 142665 (2021).
27. Taylor, M. A. et al. Future Caribbean climates in a world of rising temperatures: the 1.5 vs 2.0 dilemma. *J. Clim.* **31**, 2907–2926 (2018).
28. Liu, C. et al. Hemispheric asymmetric response of tropical cyclones to CO_2 emission reduction. *NPJ Clim. Atmos. Sci.* **7**, 83 (2024).
29. Moon, M. et al. Tropical cyclone response to ambitious decarbonization scenarios. *NPJ Clim. Atmos. Sci.* **8**, 228 (2025).
30. DeMaria, M., Sampson, C. R., Knaff, J. A. & Musgrave, K. D. Is tropical cyclone intensity guidance improving? *Bull. Am. Meteorol. Soc.* **95**, 387–398 (2014).
31. Wu, Q., Ruan, Z., Chen, D. & Lian, T. Diurnal variations of tropical cyclone precipitation in the inner and outer rainbands. *J. Geophys. Res. Atmos.* **120**, 1–11 (2015).
32. Gallo, F. et al. High-resolution regional climate model projections of future tropical cyclone activity in the Philippines. *Int. J. Climatol.* **39**, 1181–1194 (2019).
33. Lee, H. et al. Future change in tropical cyclone activity over the western North Pacific in CORDEX-East Asia multi-RCMs forced by HadGEM2-AO. *J. Clim.* **32**, 5053–5067 (2019).
34. Zhang, C. & Wang, Y. Projected future changes of tropical cyclone activity over the western North and South Pacific in a 20-km-mesh regional climate model. *J. Clim.* **30**, 5923–5941 (2017).
35. Wehner, M. F., Reed, K. A., Loring, B., Stone, D. & Krishnan, H. Changes in tropical cyclones under stabilized 1.5 and 2.0 °C global warming scenarios as simulated by the community atmospheric model under the HAPPI protocols. *Earth Syst. Dyn.* **9**, 187–195 (2018).
36. Wen, S. et al. Estimation of economic losses from tropical cyclones in China at 1.5 °C and 2.0 °C warming using the regional climate model COSMO-CLM. *Int. J. Climatol.* **39**, 724–737 (2019).
37. Delfino, R. J., Vidale, P. L., Bagtasa, G. & Hodges, K. Response of damaging Philippines tropical cyclones to a warming climate using the pseudo global warming approach. *Clim. Dyn.* **61**, 3499–3523 (2023).
38. Tran, T. L., Ritchie, E. A., Perkins-Kirkpatrick, S. E., Bui, H. & Luong, T. M. Future changes in tropical cyclone exposure and impacts in Southeast Asia from CMIP6 pseudo-global warming simulations. *Earth's Future* **10**, e2022EF003118 (2022).
39. Tran, T. L., Ritchie, E. A., Perkins-Kirkpatrick, S. E., Bui, H. & Luong, T. M. Variations in rainfall structure of western North Pacific landfalling tropical cyclones in the warming climates. *Earth's Future* **12**, e2024EF004808 (2024).
40. Bevacqua, E., Schleussner, C.-F. & Zscheischler, J. A year above 1.5 °C signals that Earth is most probably within the 20-year period that will reach the Paris agreement limit. *Nat. Clim. Change* **15**, 262–265 (2025).
41. Rückamp, M., Falk, U., Frieler, K., Lange, S. & Humbert, A. The effect of overshooting 1.5 °C global warming on the mass loss of the Greenland ice sheet. *Earth Syst. Dyn.* **9**, 1169–1189 (2018).
42. Lee, M., Min, S.-K. & Cha, D.-H. Convection-permitting simulations reveal expanded rainfall extremes of tropical cyclones affecting South Korea due to anthropogenic warming. *NPJ Clim. Atmos. Sci.* **6**, 176 (2023).
43. Cho, W. et al. Effects of topography and sea surface temperature anomalies on heavy rainfall induced by Typhoon Chaba in 2016. *Geosci. Lett.* **9**, 29 (2022).
44. Osuri, K. K., Mohanty, U., Routray, A., Kulkarni, M. A. & Mohapatra, M. Customization of WRF-ARW model with physical parameterization schemes for the simulation of tropical cyclones over North Indian Ocean. *Nat. Hazards* **63**, 1337–1359 (2012).
45. Shepherd, T. J. & Walsh, K. J. Sensitivity of hurricane track to cumulus parameterization schemes in the WRF model for three intense tropical cyclones: impact of convective asymmetry. *Meteorol. Atmos. Phys.* **129**, 345–374 (2017).
46. Huffman, G. J., Bolvin, D. T., Nelkin, E. J. & Tan, J. Integrated multi-satellite retrievals for GPM (IMERG) technical documentation. *NASA/GSFC Code* **612**, 2019 (2015).
47. Nie, J., Sobel, A. H., Shaevitz, D. A. & Wang, S. Dynamic amplification of extreme precipitation sensitivity. *Proc. Natl. Acad. Sci. USA* **115**, 9467–9472 (2018).
48. Emanuel, K., DesAutels, C., Holloway, C. & Korty, R. Environmental control of tropical cyclone intensity. *J. Atmos. Sci.* **61**, 843–858 (2004).
49. Kimball, S. K. A modeling study of hurricane landfall in a dry environment. *Mon. Weather Rev.* **134**, 1901–1918 (2006).
50. Zheng, M. & Wang, C. Interdecadal changes of tropical cyclone intensity in the South China Sea. *Clim. Dyn.* **60**, 409–425 (2023).
51. Hartmann, D. L., Blossey, P. N. & Dygert, B. D. Convection and climate: what have we learned from simple models and simplified settings? *Curr. Clim. Change Rep.* **5**, 196–206 (2019).
52. Deng, H., Ji, Z., Zhu, X. & Dong, W. Future changes of tropical cyclone activity over the west Pacific under the 1.5 °C and 2 °C limited warming scenarios using a detecting and tracking algorithm. *Front. Environ. Sci.* **10**, 1046890 (2022).
53. Chen, J. et al. Impacts of climate change on tropical cyclones and induced storm surges in the Pearl River delta region using pseudo-global-warming method. *Sci. Rep.* **10**, 1965 (2020).
54. Park, J. et al. Impact of cloud microphysics schemes on tropical cyclone forecast over the western North Pacific. *J. Geophys. Res. Atmos.* **125**, e2019JD032288 (2020).
55. Kwun, J. H., Kim, Y. K., Seo, J. W., Jeong, J. H. & You, S. H. Sensitivity of MM5 and WRF mesoscale model predictions of surface winds in a typhoon to planetary boundary layer parameterizations. *Nat. hazards* **51**, 63–77 (2009).
56. Cha, D. H., Jin, C. S., Lee, D. K. & Kuo, Y. H. Impact of intermittent spectral nudging on regional climate simulation using Weather Research and Forecasting model. *J. Geophys. Res. Atmos.* **116**, D10103 (2011).
57. Gentry, M. S. & Lackmann, G. M. Sensitivity of simulated tropical cyclone structure and intensity to horizontal resolution. *Mon. Weather Rev.* **138**, 688–704 (2010).
58. Hon, K.-K. Tropical cyclone track prediction using a large-area WRF model at the Hong Kong observatory. *Trop. Cyclone Res. Rev.* **9**, 67–74 (2020).
59. Qin, X., Duan, W. & Xu, H. Sensitivity to tendency perturbations of tropical cyclone short-range intensity forecasts generated by WRF. *Adv. Atmos. Sci.* **37**, 291–306 (2020).
60. Jin, C.-S. et al. Evaluation of climatological tropical cyclone activity over the western North Pacific in the CORDEX-East Asia multi-RCM simulations. *Clim. Dyn.* **47**, 765–778 (2016).

61. Kim, D., Jin, C.-S., Ho, C.-H., Kim, J. & Kim, J.-H. Climatological features of WRF-simulated tropical cyclones over the western North Pacific. *Clim. Dyn.* **44**, 3223–3235 (2015).
62. Hersbach, H. et al. The ERA5 global reanalysis. *Q. J. R. Meteorol. Soc.* **146**, 1999–2049 (2020).
63. Hong, S.-Y. & Lim, J.-O. J. The WRF single-moment 6-class microphysics scheme (WSM6). *Asia Pac. J. Atmos. Sci.* **42**, 129–151 (2006).
64. Iacono, M. J. et al. Radiative forcing by long-lived greenhouse gases: calculations with the AER radiative transfer models. *J. Geophys. Res. Atmos.* **113**, D13103, (2008).
65. Hong, S.-Y., Noh, Y. & Dudhia, J. A new vertical diffusion package with an explicit treatment of entrainment processes. *Mon. Weather Rev.* **134**, 2318–2341 (2006).
66. Feser, F. & von Storch, H. A dynamical downscaling case study for typhoons in Southeast Asia using a regional climate model. *Mon. Weather Rev.* **136**, 1806–1815 (2008).
67. von Storch, H., Langenberg, H. & Feser, F. A spectral nudging technique for dynamical downscaling purposes. *Mon. Weather Rev.* **128**, 3664–3673 (2000).
68. Taniguchi, K. & Tajima, Y. Variations in extreme wave events near a South Pacific Island under global warming: case study of tropical cyclone Tomas. *Prog. Earth Planet. Sci.* **7**, 8 (2020).
69. Tropea, B. & Stewart, R. Assessing past and future hazardous freezing rain and wet snow events in Manitoba, Canada using a pseudo-global warming approach. *Atmos. Res.* **259**, 105656 (2021).
70. Moon, J., Cha, D. H., Lee, M. & Kim, J. Impact of spectral nudging on real-time tropical cyclone forecast. *J. Geophys. Res. Atmos.* **123**, 12,647–612,660 (2018).
71. Huang, W., Xie, L., Hong, F. & Zhu, J. Assessing the effectiveness of spectral nudging in improving tropical cyclone track simulations over the western North Pacific using the WRF model. *Atmosphere* **16**, 1028 (2025).
72. Eyring, V. et al. Overview of the coupled model intercomparison project phase 6 (CMIP6) experimental design and organization. *Geosci. Model Dev.* **9**, 1937–1958 (2016).
73. O'Neill, B. C. et al. The scenario model intercomparison project (ScenarioMIP) for CMIP6. *Geosci. Model Dev.* **9**, 3461–3482 (2016).
74. Frei, C., Schär, C., Lüthi, D. & Davies, H. C. Heavy precipitation processes in a warmer climate. *Geophys. Res. Lett.* **25**, 1431–1434 (1998).
75. Kawase, H. et al. Intermodel variability of future changes in the Baiu rainband estimated by the pseudo global warming downscaling method. *J. Geophys. Res. Atmos.* **114**, D24110 (2009).
76. Rasmussen, R. et al. High-resolution coupled climate runoff simulations of seasonal snowfall over Colorado: a process study of current and warmer climate. *J. Clim.* **24**, 3015–3048 (2011).
77. Schär, C., Frei, C., Lüthi, D. & Davies, H. C. Surrogate climate-change scenarios for regional climate models. *Geophys. Res. Lett.* **23**, 669–672 (1996).
78. Takemi, T., Ito, R. & Arakawa, O. Robustness and uncertainty of projected changes in the impacts of Typhoon Vera (1959) under global warming. *Hydrol. Res. Lett.* **10**, 88–94 (2016).
79. Lackmann, G. M. Hurricane Sandy before 1900 and after 2100. *Bull. Am. Meteorol. Soc.* **96**, 547–560 (2015).
80. Takayabu, I. et al. Climate change effects on the worst-case storm surge: a case study of Typhoon Haiyan. *Environ. Res. Lett.* **10**, 064011 (2015).
81. Lackmann, G. M. The south-central US flood of May 2010: present and future. *J. Clim.* **26**, 4688–4709 (2013).

Acknowledgements

This study was supported by the National Research Foundation of Korea (NRF) grant funded by the Korean Government (MSIT) (NRF2021R1A2C3007366), Korea Meteorological Administration Research and Development Program (RS-2024-00403386), and Research and Development Program of the Korea Institute of Energy Research (C6-2403-15).

Author contributions

S.-K.M. designed the research. M.L. conducted WRF model experiments, analyzed the outputs, and wrote the initial manuscript. S.-K.M. and D.-H.C. contributed to the analysis and the manuscript writing.

Competing interests

S.-K.M. is an Editorial Board Member for *Communications Earth and Environment*, but was not involved in the editorial review of, nor the decision to publish this article. The authors declare no other competing interests.

Additional information

Supplementary information The online version contains Supplementary material available at https://doi.org/10.1038/s43247-026-03317-1.

Correspondence and requests for materials should be addressed to Seung-Ki Min.

Peer review information *Communications Earth and Environment* thanks Zheng-Hang Fu and the other anonymous reviewer(s) for their contribution to the peer review of this work. Primary handling editors: Chao He and Nicola Colombo. A peer review file is available.